An $\mathcal{L}_1$ Adaptive Control Augmentation for a Lift-Plus-Cruise Vehicle

Andrew Patterson*, Kasey Ackerman*, Michael Acheson†, Irene Gregory‡[1]
[1]*NASA Langley Research Center, Hampton, VA, 23666, USA*

This paper presents an $\mathcal{L}_1$ adaptive control augmentation for a Lift-Plus-Cruise (L+C) vehicle. This class of vehicles operates in three flight modes with different dynamic behavior: vertical, transition, and forward flight. A robust uniform controller is used as a baseline to stabilize the system throughout these flight modes. The uniform controller is a linear control law designed around trim conditions of the aircraft and includes control allocation to achieve the desired forces and moments on the vehicle. The $\mathcal{L}_1$ control augmentation is designed for each of these trim conditions to compensate for the nonlinear time- and state-dependent uncertainties in the vehicle dynamics. The augmented control output is then added to the desired force and moment commands on the vehicle. Simulation results demonstrate the effectiveness of control augmentation for reducing the effects of unmodeled dynamics, reduced actuator effectiveness, and time-dependent disturbances. Effectiveness is demonstrated through tracking error metrics.

I. Introduction

As populations in urban centers grow, new methods and vehicles are being developed to help decrease transportation bottlenecks. One method of increasing urban freedom of movement is by making increased use of airspace capacity with new vehicle configurations. This concept is called Urban Air Mobility (UAM) and is an Advanced Air Mobility (AAM) concept to augment the existing short connection, intra- and inter-city flights typically provided by small private helicopters or fixed-wing aircraft. However, traditional aircraft are limited by their configuration. Airplanes require a long runway, limiting the number of areas that can be connected. Helicopters are often loud and inefficient, making long connections difficult. New UAM vehicle designs strike a balance between these configurations by including multiple modes, achieving both the flexibility of vertical take-off and landing (VTOL) and the efficiency of wing-borne forward flight. Such vehicles are expected to improve public transportation, last-mile delivery, and on-demand mobility, operating over a wide range of locations, ranges, and price points.

One such vehicle configuration is the Lift-Plus-Cruise (L+C) vehicle, which has vertical propellers for VTOL operation, and a fixed-wing for efficient forward flight [1]. One benefit of this configuration is that the wing and propulsors are all fixed, meaning the vehicle kinematics are not changing during flight. This reduces the number of failure points. Instead, the direction of force on the vehicle is changed by using a combination of both vertical and horizontal propellers. The model considered in this work is shown in Figure 1. Notice that the VTOL operation is achieved using the eight vertical propellers while level forward flight is driven by a pusher propeller.

While this vehicle does not need to account for changing kinematics, the transition between vertical and forward flight is still complicated. Control of this vehicle is performed using a combination of the propellers and aerodynamic surfaces. Control allocation methods are used to connect motion in a desired direction to the control surfaces, such as the propellers and aerodynamic surfaces. This control allocation is demonstrated in Ref. [2], where the authors present a joint allocation and control design method that unifies the controller design for all operating modes of a transitioning vehicle. This control method is extended to include allocation constraints and applied to the L+C vehicle of this work in Ref. [3].

While the robust uniform control method performs well during nominal operation of the vehicle, these vehicles will need to be able to react and respond to many different contingencies and uncertainties during flight [4]. Uncertainties that may affect the vehicle could be unmodeled dynamics or reduced actuator effectiveness. Furthermore, the aerodynamics of this transition region are influenced by the propulsive interactions between the propellers and the wings. Advances in aerodynamic modeling for this class of vehicle can be found in Refs. [5–7]. Any errors or approximations made during

*Research Engineer, Dynamic Systems and Control Branch
*Research Engineer, Dynamic Systems and Control Branch
†Aerospace Technologist, Dynamic Systems and Control Branch
‡NASA Senior Technologist for Advanced Control Theory and Application, Fellow AIAA

Fig. 1 Rendering of a Lift+Cruise NASA reference configuration.

modeling and control design may appear as time-dependent disturbances. Additionally, external disturbances, such as winds, can perturb the normal operation of the vehicle.

To compensate for the dynamic uncertainties that affect the normal operation of the vehicle, we propose an $\mathcal{L}_1$ adaptive controller designed to augment the baseline robust uniform controller on the L+C vehicle. The $\mathcal{L}_1$ controller is chosen because of its proven flight history, ability to adapt quickly to disturbances, and robustness. Furthermore, the structure of the $\mathcal{L}_1$ controller decouples the estimation and control contributions to preserve the robustness of the closed loop system [8]. The $\mathcal{L}_1$ adaptive controller has been successfully applied to many traditional aircraft, such as a 5.5% scale transport aircraft [9], the Calspan Learjet [10], and an F-16 [11]. Other applications include augmentations for small unmanned aircraft [12]. The $\mathcal{L}_1$ controller has also been designed for a L+C vehicle by the authors of Ref. [13], where independent projection-based $\mathcal{L}_1$ controllers are designed to augment nonlinear dynamic inversion controllers on angular rate commands.

In this work, we design a piecewise-constant (PWC) $\mathcal{L}_1$ adaptive controller to augment a robust uniform control baseline. This augmentation will adapt and compensate for uncertainties in not only the angular rates but also the linear velocities of the vehicle. Furthermore, rather than considering all the axes of the system to be independent, the structure of the uniform control baseline captures the interactions between the linear and rotational velocities. This allows the uncertainties in this interaction to be captured. Further, the PWC implementation of the controller does not rely on the projection operator and optimization procedure to adapt to uncertainty. Rather, the adaptation is determined by the PWC adaptation law, which has proven flight history, better numerical robustness, and can be quickly computed online [14]. The performance of this controller is demonstrated in simulation.

In this paper, we present: 1) an architecture for uncertainty compensation in both rotational and linear dynamics of a transitional UAM vehicle; 2) a PWC $\mathcal{L}_1$ design for online implementation; 3) verification though simulation of a high fidelity model. In Section II the L+C vehicle dynamics are described. In Section III the baseline controller is introduced. Section IV develops the $\mathcal{L}_1$ control augmentation and simulation results are shown in Section V. Finally, Section VI presents a summary of contributions and future work.

II. Vehicle Dynamics

The L+C aircraft shown in Figure 1 is a conceptual VTOL aircraft developed by NASA [1]. The VTOL phases of flight are handled by the eight vertically mounted propellers, which provide lifting thrust. After transition to forward flight, the pusher propeller, attached to the tail, provides the forward thrust necessary to maintain flight. During transition, a combination of the propellers is used to transfer the lift generation from the vertical propellers to the wings or vice versa.

We consider three frames of reference in this work. The first is the inertial frame, defined by the North-East-Down (NED) vectors. The second is the body frame, centered at the vehicle center of mass. The body frame is a right-handed coordinate system with the x-axis pointing out the nose of the aircraft and the z-axis pointing down. The rotation from the body frame to the inertial frame is given by the rotation matrix $\mathrm{R} \in \mathrm{SO}(3)$. The rotation matrix can be parameterized in terms of Euler angles, using the 3-2-1 rotation sequence [15]. The vector of Euler angles is composed of roll, pitch and yaw, denoted $\eta = [\phi,\ \theta,\ \psi]^\top$, respectively. The third frame of reference, called the heading frame, is the inertial frame rotated around its z-axis by ψ. The rotation from the body to heading frame is denoted $\bar{\mathrm{R}}$. The overbar indicates that an associated vector or map is in the heading frame.

The rotational dynamics of the aircraft are given by $\dot{\eta} = \mathrm{S}\omega$, where $\omega = [p,\ q,\ r]^\top$ is the vector of angular rates in

the body frame and

$$S = \begin{bmatrix} 1 & \sin\phi\tan\theta & \cos\phi\tan\theta \\ 0 & \cos\phi & -\sin\phi \\ 0 & \sin\phi/\cos\theta & \cos\phi/\cos\theta \end{bmatrix}. \tag{1}$$

The full nonlinear dynamics are then given by the following equations:

$$\begin{aligned} \dot{p} &= \mathbf{v}, \\ \dot{\eta} &= \mathrm{S}\omega, \\ \dot{\bar{\mathbf{v}}} &= -\dot{\psi}\mathrm{e}_3 \times \bar{\mathbf{v}} + g + m^{-1}\bar{F}\left(X, u\right), \\ J\dot{\omega} &= -\omega \times J\omega + \tau\left(X, u\right), \end{aligned} \tag{2}$$

where $\mathbf{v}$ is the inertial frame velocity of the vehicle, $\bar{\mathbf{v}} = [\bar{u},\ \bar{v},\ \bar{w}]^\top$ is the heading frame velocity of the vehicle, e_3 is a unit vector aligned with the inertial z-axis, g is gravitational acceleration, m is the vehicle mass, u is the vector of control inputs, J is the vehicle inertia, $X = [p,\ \eta,\ \bar{\mathbf{v}},\ \omega]^\top$ is the full state vector, and the functions $\bar{F}$ and τ are aerodynamic propulsive models for the force and torque generated by the actuators. The development of these aerodynamic functions is provided in Ref. [7].

III. Baseline Controller

The baseline controller is designed for a set of operating conditions within the flight envelope of the vehicle. The controller is designed by linearizing the dynamics at the operating condition and then finding 1) an appropriate allocation for the actuators and 2) solving for the minimum energy feedback gains to achieve the desired performance with the chosen allocation. The full description of this method can be found in Ref. [2] and it is applied to the L+C vehicle in Ref. [3].

To simplify the linearization process, it is assumed that $\dot{\psi} \equiv 0$. This condition implies that the vehicle is not turning, removing the associated cross product term in the velocity dynamics of Equation 2. The second assumption is that the longitudinal and lateral dynamics are decoupled. Thus, the linearized dynamics can be written as a set of linear equations:

$$\begin{aligned} \dot{x}_{\mathrm{lon}} &= A_{\mathrm{lon}}x_{\mathrm{lon}} + B_{\mathrm{lon}}u, \\ \dot{x}_{\mathrm{lat}} &= A_{\mathrm{lat}}x_{\mathrm{lat}} + B_{\mathrm{lat}}u, \end{aligned} \tag{3}$$

where A and B are the system and control matrices produced by the linearization process, $x_{\mathrm{lon}} = [\bar{u},\ \bar{w},\ q]^\top$, $x_{\mathrm{lat}} = [\bar{v},\ p,\ r]^\top$, and u is a vector of actuator commands for the propellers, ailerons, flaps, elevators and rudder.

For both lateral and longitudinal channels, the control matrix of the linearized system can be used to compute a generalized control input, μ, which expresses acceleration commands for the vehicle. This input change is given, for the longitudinal channel, by the equation $\mu_{\mathrm{lon}} = B_{\mathrm{lon}}u_{\mathrm{lon}}$. The value of u_{lon}, given a generalized control input μ_{lon}, can then be computed using the generalized weighted inverse of B_{lon}:

$$u_{\mathrm{lon}} = W_{\mathrm{lon}}^{-1}B_{\mathrm{lon}}^\top\left(B_{\mathrm{lon}}W_{\mathrm{lon}}^{-1}B_{\mathrm{lon}}^\top\right)^{-1}\mu_{\mathrm{lon}}, \tag{4}$$

where W_{lon} is a weighting matrix. The full control command of the vehicle is then computed, $u = u_{\mathrm{lon}} + u_{\mathrm{lat}}$. Note that the lateral and longitudinal commands, u_{lat} and u_{lon}, are generated by separate controllers but both contribute to all the actuator commands. The generalized control inputs, μ_{lat} and μ_{lon}, are both independently generated and contribute directly to independent states. By recasting the system dynamics in terms of these acceleration commands, we can write the performance system as:

$$\begin{aligned} \dot{x}_{\mathrm{lon}} &= A_{\mathrm{lon}}x_{\mathrm{lon}} + \mu_{\mathrm{lon}}, \\ \dot{x}_{\mathrm{lat}} &= A_{\mathrm{lat}}x_{\mathrm{lat}} + \mu_{\mathrm{lat}}. \end{aligned} \tag{5}$$

This computation allows the system actuators to be allocated based on desired force and moment commands and occurs at each controller time-step.

The baseline controller calculates the desired control accelerations using this model such that

$$\mu_{\text{lon}} = -\begin{bmatrix} K_{i,\text{lon}}, & K_{x,\text{lon}} \end{bmatrix} \begin{bmatrix} x_{i,\text{lon}} \\ x_{\text{lon}} \end{bmatrix}, \tag{6}$$

where $\dot{x}_{i,\text{lon}} = x_{i,\text{lon}} - R_{\text{lon}}$ describes the integrated error of the system and r_{lon} is a reference target provided by a trajectory generation or guidance system. These gains are chosen using LQR methods described in Refs. [2] and [3].

IV. $\mathcal{L}_1$ Design

The ideal performance of the Lift+Cruise vehicle is described by the nonlinear equations in Equation (2). These equations are linearized at multiple operating points and the baseline controller is designed based on the simplified performance dynamics given in Equation (5). For clarity, we drop the 'lat' and 'lon' subscripts from the performance system and consider both cases simultaneously:

$$\dot{x}(t) = Ax(t) + \mu(t) + \sigma(t, x(t)), \tag{7}$$

where t is time and $\sigma(t, x(t))$ represents the time and state dependent uncertainties affecting the system. Notice that all uncertainties in this formulation can be directly compensated for through the command μ.

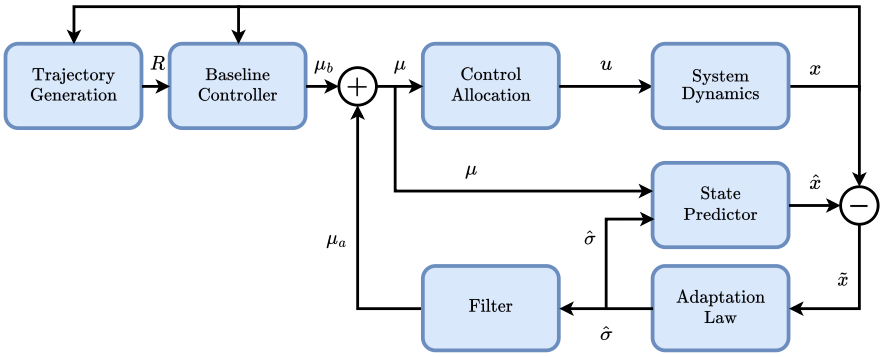

Fig. 2 $\mathcal{L}_1$ adaptive control augmentation.

To compensate for these uncertainties, this paper considers an $\mathcal{L}_1$ adaptive control augmentation, as shown in Figure 2. The control augmentation is composed of a state predictor, an adaptation law, and a unity DC gain low-pass filter. The adaptive control law produces an additional command, μ_a, which is added to the baseline command, μ_b, to compensate for the uncertainty $\sigma(t, x(t))$.

A. State Predictor

The state predictor is used to predict the state of a reference model based on the applied control input and estimate of system uncertainty. The state predictor dynamics are given by the equation:

$$\dot{\hat{x}}(t) = Ax(t) + \mu(t) + \hat{\sigma}(t) + L\tilde{x}(t), \tag{8}$$

where $\hat{x}$ is the state estimate, $\hat{\sigma}(t)$ is the uncertainty estimate, L is a negative semi-definite observer gain matrix chosen such that $A_s := A + L$ is a Hurwitz matrix, and $\tilde{x} := \hat{x} - x$. The gain L is a design parameter that can be chosen to improve the convergence of the state predictor dynamics.

B. Adaptation Law

The adaptation law can be implemented with a feedback gain, rather than a continuously evolving dynamic system, when considering a linear state-predictor reference model. This formulation is called the piecewise-constant adaptation law since the uncertainty is assumed to be constant on the scale of a single controller time-step. This assumption allows the uncertainty estimate to be computed using the analytic solution to the uncertainty dynamics. This analytic solution frees the designer from having to choose the adaptation gain or evaluate additional dynamic equations numerically.

From these state predictor dynamics, we can compute the adaptation law gain with the equation:

$$K_a = -\left(A_s^{-1}\left(\text{expm}(A_s T_s) - \mathbb{I}\right)\right)^{-1} \text{expm}(A_s T_s), \tag{9}$$

where $\mathbb{I}$ is an identity matrix of appropriate dimension, and T_s is the execution rate of the adaptive controller. Note that there are no B matrix terms in the adaptation law since the state predictor inputs have a direct correspondence with the states.

The state uncertainty is then computed at each controller time step, $i \in \mathbb{N}$:

$$\hat{\sigma}(t) = \hat{\sigma}(iT_s) = K_a \tilde{x}(iT_s), \quad \forall t \in [iT_s, (i+1)T_s). \tag{10}$$

C. Control Law

The control law is given by the frequency-domain equation:

$$\mu_a(s) = C(s)\hat{\sigma}(s) \tag{11}$$

where $s \in \mathbb{C}$ and $C(s)$ is a low-pass filter of appropriate dimension satisfying $C(0) = \mathbb{I}$. This filter prevents high frequency uncertainty estimates from being sent into the control channel. A more complete description of the filter's connection to the robustness and performance of the system can be found in Refs. [14, 16]. In this work we consider a Butterworth low-pass filter structure and optimize over cutoff frequency ω_0 and model orders, with penalties for high order filters.

V. Results

The simulation is performed in the high-fidelity simulator used for the development of the benchmark problems described in [4]. The simulator includes several vehicle models, and results are shown for the Lift+Cruise vehicle model. To demonstrate performance in multiple flight modes, we will consider trajectories that cover VTOL, transition, and forward flight. One such trajectory is shown in Figure 3. In this figure, the reference trajectory is shown as the black line. The baseline tracking performance is shown as a blue line. The ground tracks are shown as dashed lines on the ground plane. During the first leg of the flight, the vehicle takes off vertically up to about 700 ft altitude and then begins to transition to forward flight before reaching the cruise altitude of 1000 ft. Finally, the vehicle turns in forward flight and increases speed before beginning a final descent. This trajectory demonstrates the different phases of flight of the vehicle how each controller performs in a specific mission.

A. Performance Metrics

Performance is captured in terms of two metrics. The first metric is mean velocity tracking error (MVTE). The second metric is the maximum velocity tracking error (XVTE). These metrics are defined by the equations:

$$\begin{aligned} \text{MVTE}(r, \bar{\mathbf{v}}) &= \text{mean}\left(\|r_v(T) - \bar{\mathbf{v}}(T)\|_2\right) \\ \text{XVTE}(r, \bar{\mathbf{v}}) &= \max\left(\|r_v(T) - \bar{\mathbf{v}}(T)\|_2\right), \end{aligned} \tag{12}$$

where r_v is the subset of the guidance command containing velocity targets in the heading frame, T is a discrete set of times where the vehicle state is evaluated, the norm,$\|\cdot\|_2$, is taken over the spatial dimensions, and the mean and maximum operations are evaluated over the temporal dimensions.

B. Nominal Performance

To isolate and compare the performance of baseline and adaptive controllers in each phase of flight, we consider seven experiments. These experiments are tabulated in Table 1. All experiments take place over the span of 50 seconds, allowing both the transient and steady-state performance to be captured. The first experiment targets the hover performance of the vehicle by commanding a position hold. Experiments 2-4 demonstrate performance during forward flight, tracking a constant velocity target. The final set of experimental trajectories capture the dynamic performance of the vehicle. These trajectories are transitions from hover mode, with zero forward velocity, to forward flight with different forward velocities. The fixed duration of 50 seconds requires faster acceleration and faster transitions for subsequent experiments.

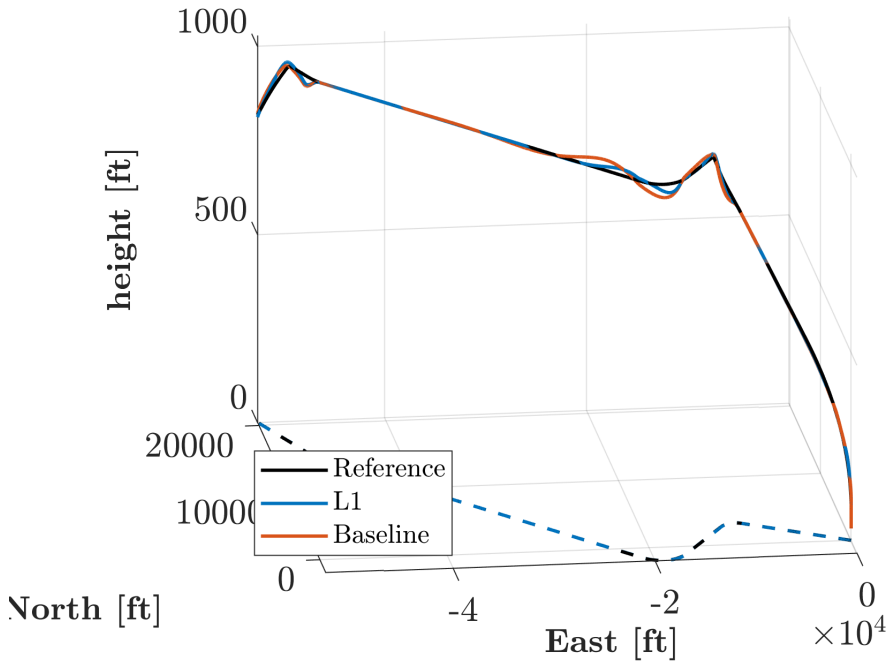

Fig. 3 Spatial trajectory tracking performance. The reference trajectory is shown in black, the vehicle center of mass trajectory is shown in blue for the $\mathcal{L}_1$ controller, and the trajectory flown by the baseline controller is shown in red. The dashed lines are the ground track lines for each trajectory.

Exp. No.	Description	Percent Improvement
1	Position hold	11%
2	Fwd velocity: 50 fps	8%
3	Fwd velocity: 100 fps	18%
4	Fwd velocity: 200 fps	31%
5	Accelerate: 0 to 50 fps	15%
6	Accelerate: 0 to 100 fps	21%
7	Accelerate: 0 to 200 fps	33%

Table 1 Experiment descriptions and percent improvement in mean velocity tracking performance due to adaptation. Each experiment is run for 50 seconds regardless of the trajectory being tested.

Three different types of uncertainties are considered in all experiments. The first is due to the scheduled nature of the controller. The controller is designed around an operating point but deviations from the operating point introduce parameter uncertainties that reduce the controller performance. These uncertainties will also arise when the non-turning assumption is violated. The second set of uncertainties is due to actuator dynamics. These represent unmodeled dynamics, with new states that can affect the performance of the baseline controller. In this work, we consider a first-order actuator model. The final uncertainty considered is a time-varying wind gust disturbance. The wind disturbances are implemented using a Dryden gust model [17]. At the low altitudes of flight considered, these wind gusts are approximately 30 fps wind-speed variations around a nominal 50 fps nominal wind-speed.

Each controller is benchmarked using 48 trials for each experimental configuration. The gust model is the only source of randomness in the trials and both the baseline and adaptive controllers trials are run with the same random seeds. The performance of each controller in each trial is given in terms of MVTE and XVTE. The results for each experiment are shown in Figure 4. Figure 4a shows the distribution of MVTEs from each of the runs of an experiment. These distributions are shown as histograms along the vertical axis, showing the extent of errors. In this figure we can see two trends associated with changes in experiment conditions. The most obvious is associated with the speed of the aircraft. The highest speed is held during Experiment 4 and we see that it has the highest average MVTE across all trials and the largest distribution of errors. The second trend is in the performance of the $\mathcal{L}_1$ adaptive controller, which performs better in all experiments. We can note that the $\mathcal{L}_1$ controller exhibits better behavior in terms of average MVTE across all trials for each experiment: the spread of the MVTE histogram is tighter, and the increase in vehicle velocity leads to a greater increase in error for the baseline than the $\mathcal{L}_1$ controller. This final trend leads to the $\mathcal{L}_1$ controller performing better in almost all trials of Experiments 4 and 7 than the best-performing trial for the baseline controller. The percent improvement of the $\mathcal{L}_1$ controller over the baseline controller in terms of average MVTE is given in Table 1.

The XVTE is shown in Figure 4b. Note that while the trend of increasing error with increasing velocity continues, the maximum errors are more spread out and improvement of the adaptive controller is less obvious at lower velocities. This difference in XVTE is likely due to transient behavior where the initial compensation for the constant wind term appears as an error spike.

The position tracking error caused by these velocity errors is shown in Figure 5. In this figure, the average position tracking error trajectory is shown for Experiment 4. This trajectory is a pointwise-in-time average of all the position error trajectories from all of the trials in Experiment 4. Here we can see that while the MVTE and XVTE are comparable, the peak position error is almost doubled for the baseline controller.

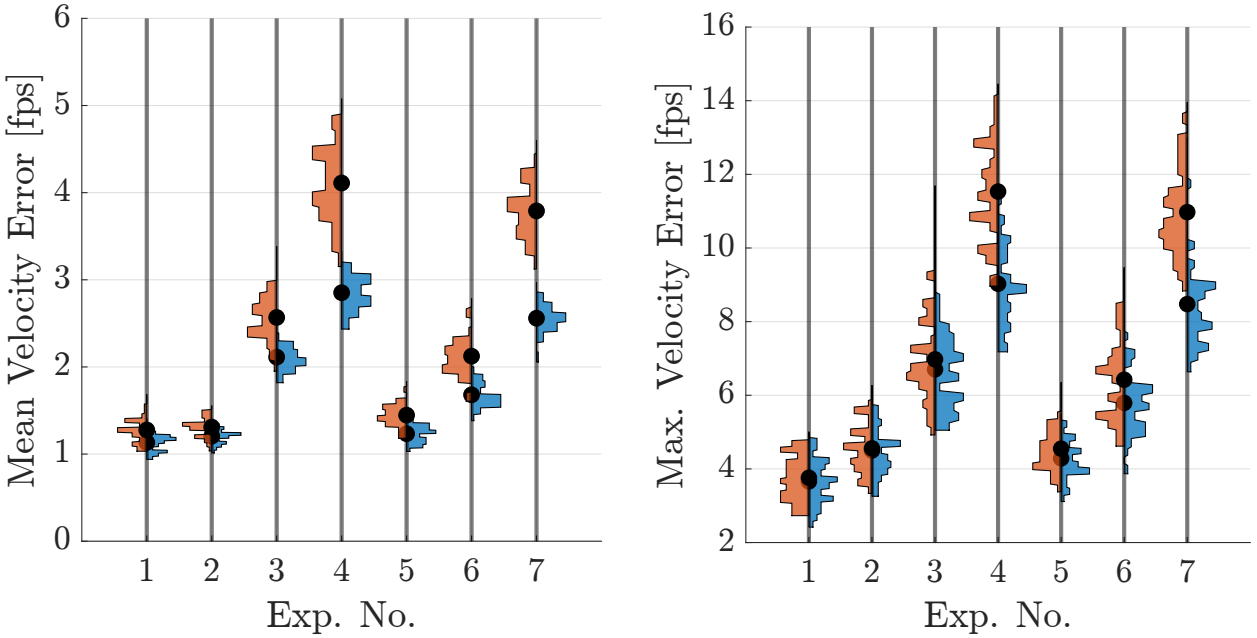

(a) Mean velocity tracking error for each trial.

(b) Maximum velocity tracking error for each trial.

Fig. 4 Nominal performance plots. The blue histograms are associated with the $\mathcal{L}_1$ controller and the red histograms are associated with the baseline controller. The black point marks the average of the distribution.

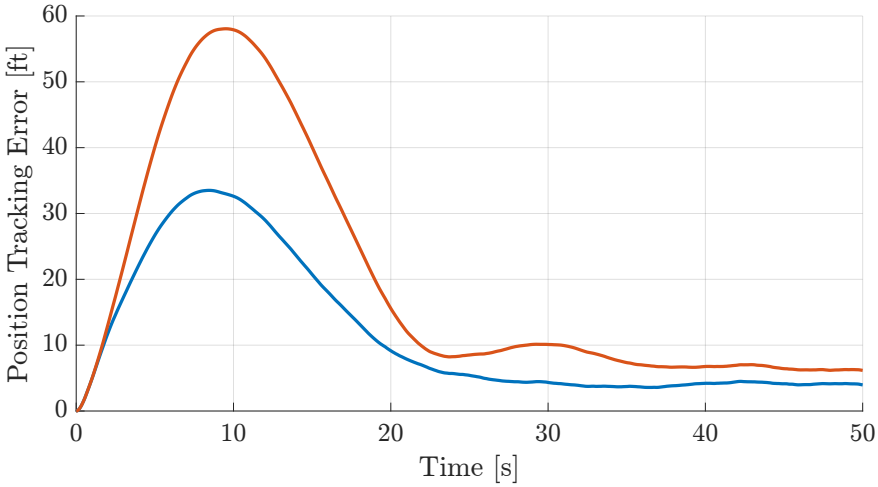

Fig. 5 Position tracking error. The blue line shows the $\mathcal{L}_1$ controller tracking error and the red line represents the baseline error trajectory.

C. Rotor Failure Compensation

The Lift+Cruise configuration shown in Figure 1 has nine propellers, eight lifting propellers and one pusher propeller. One benefit of having a large number of propellers is redundancy, allowing the vehicle to compensate for failures. In this section, we will demonstrate the $\mathcal{L}_1$ adaptive controller compensating for sudden rotor failures.

One limitation of traditional fault estimation and re-allocation methods is that correctly identifying a fault can take time, during which the vehicle is unstable. Adaptive control can reduce the effect of the failure, maintaining stability while fault detection algorithms are running. To demonstrate this capability, we consider a failure during Experiment 3, where the vehicle is flying forward at 100 fps in turbulent conditions. Two seconds into this experiment, propellers two and four lose power and their rotation rate drops. These propellers are located in the front row of propellers, directly to the left and right of the cabin. The time-history of engine speeds is shown in Figure 6 when flown with the $\mathcal{L}_1$ controller. These propellers are used for damping out the longitudinal oscillatory modes of the aircraft before the vehicle is moving fast enough for the control surfaces to be fully effective. When using the baseline controller only, losing these propellers at this time, causes the vehicle to go unstable.

When the experiment is run with the $\mathcal{L}_1$ controller, the vehicle is able to compensate for the loss of these two propellers and maintain stability. The velocity tracking error time-history is shown in Figure 7. Recall that the average XVTE for Experiment 3 is around 7 fps, in this figure we note that the vehicle has an initial jump in error to about 6 fps then failure leads subsequent larger spikes up to almost 11 fps. Despite these errors, the vehicle is stable and the error converges for an MVTE of 3.5 fps.

VI. Conclusion

This paper demonstrates the design and evaluation of an $\mathcal{L}_1$ adaptive controller within the uniform control framework. The $\mathcal{L}_1$ controller augments the baseline uniform controller at the level of the desired forces and moments, allowing it to be easily used with multiple aircraft configurations without changing the controller structure. The $\mathcal{L}_1$ controller reduces the effect of disturbances and uncertainties during flight, as shown in a set of experiments performed in simulation. The $\mathcal{L}_1$ controller performs better than the baseline alone in all cases and is demonstrated to maintain stability in a failure case where the baseline goes unstable.

Future work will consider integrating $\mathcal{L}_1$ with a nonlinear baseline controller and will include compensation for learned information during flight.

Acknowledgments

The authors would like to thank Jacob Cook for his help with the uniform control framework, Thomas Britton for his help with simulation integration, and Steven Snyder for his $\mathcal{L}_1$ discussions. This research is supported by the NASA

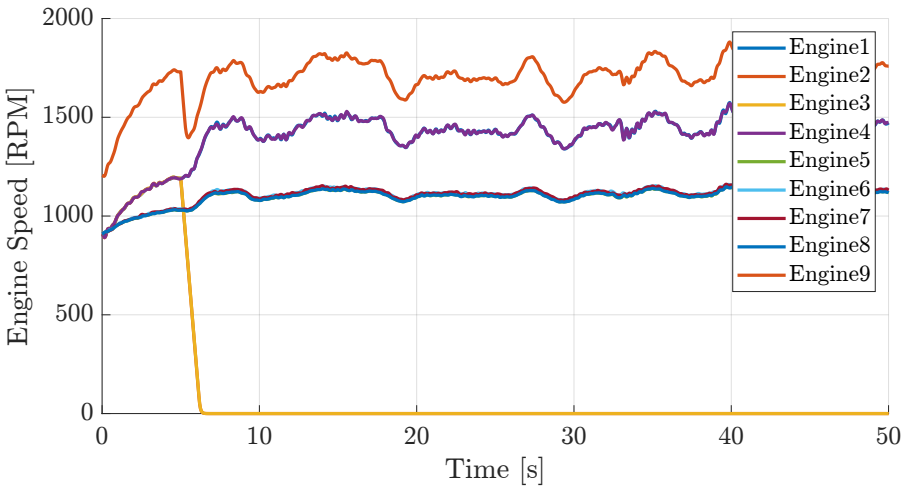

Fig. 6 Engine speed time-history during Experiment 3 run with the $\mathcal{L}_1$ adaptive controller and a failure of engines two and three. Engines are numbered left-to-right and front-to-back, so that engine 9 is the pusher propeller.

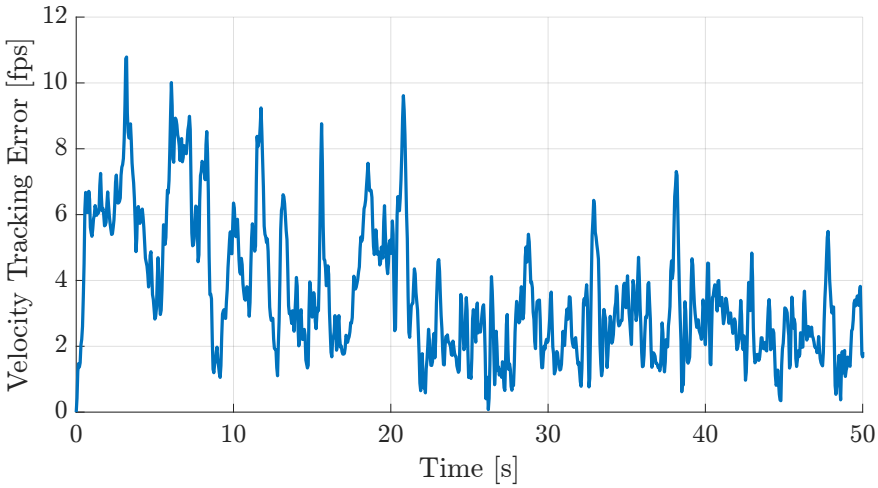

Fig. 7 Velocity error time history. The blue line shows the $\mathcal{L}_1$ controller tracking error. The baseline performance is not shown, since the vehicle quickly goes unstable.

Transformational Tools and Technologies project.

References

[1] Silva, C., Johnson, W., Anticlif, K. R., and Patterson, M. D., "VTOL Urban Air Mobility Concept Vehicles for Technology Development," *AIAA Aviation*, Atlanta, GA, USA, 2018. AIAA 2018-3847.

[2] Cook, J., and Gregory, I., "A Robust Uniform Control Approach for VTOL Aircraft," *VFS Autonomous VTOL Technical Meeting and Electric VTOL Symposium*, Virtual, 2021.

[3] Acheson, M., Gregory, I., and Cook, J., "Examination of Unified Control Incorporating Generalized Control Allocation," *AIAA SciTech*, Virtual, 2021. AIAA 2021-0999.

[4] Holbrook, J., Neogi, N. A., Acheson, M. J., and Gregory, I. M., "Benchmark Problem Development for Testing Maturity of Intelligent Contingency Management Tools," *AIAA SciTech*, San Diego, CA, USA and Virtual, 2022. AIAA 2022-0784.

[5] Simmons, B. M., Buning, P. G., and Murphy, P. C., "Full-Envelope Aero-Propulsive Model Identification for Lift+Cruise Aircraft Using Computational Experiments," *AIAA Aviation*, Virtual, 2021. AIAA 2021-3170.

[6] Simmons, B. M., and Murphy, P. C., "Aero-Propulsive Modeling for Tilt-Wing, Distributed Propulsion Aircraft Using Wind Tunnel Data," *AIAA Journal of Aircraft*, Vol. online, 2022.

[7] Cook, J., "A Strip Theory Approach to Dynamic Modeling of eVTOL Aircraft," *AIAA SciTech*, Virtual, 2021. AIAA 2021-1720.

[8] Hovakimyan, N., and Cao, C., $\mathcal{L}_1$ *Adaptive Control Theory: Guaranteed Robustness with Fast Adaptation*, 1st ed., SIAM, Philadelphia, PA, USA, 2010.

[9] Gregory, I., Cao, C., Xargay, E., Hovakimyan, N., and Zou, X., "$\mathcal{L}_1$ adaptive control design for NASA AirSTAR flight test vehicle," *AIAA GNC*, Chicago, IL, USA, 2009. AIAA 2009-5738.

[10] Ackerman, K. A., Xargay, E., Choe, R., Hovakimyan, N., Cotting, M. C., Jeffrey, R. B., Blackstun, M. P., Fulkerson, T. P., Lau, T. R., and Stephens, S. S., "Evaluation of an $\mathcal{L}_1$ Adaptive Flight Control Law on Calspan's Variable-Stability Learjet," *Journal of Guidance, Control, and Dynamics*, Vol. 40, No. 4, 2017, pp. 1051–1060.

[11] "Adaptive Advance: Flight tests of adaptive controller could pave way for backup protection against control loss," , 2016. http://naira.mechse.illinois.edu/upcoming-f-16-testing-featured-in-aviation-week/ Accessed: 2022-05-17.

[12] Wu, Z., Cheng, S., Ackerman, K. A., Gahlawat, A., Lakshmanan, A., Zhao, P., and Hovakimyan, N., "$\mathcal{L}_1$ Adaptive Augmentation for Geometric Tracking Control of Quadrotors," *IEEE ICRA*, Philadelphia, PA, USA, 2022, pp. 1329–1336.

[13] Wang, Z., Gong, Z., Zhang, C., and Mao, J. H. S., "Flight Test of $\mathcal{L}_1$ Adaptive Control on 120-kg-Class Electric Vertical Take-Off and Landing Vehicles," *IEEE Access*, Vol. 9, 2022, pp. 163906–163928.

[14] Xargay, E., Hovakimyan, N., and Cao, C., "$\mathcal{L}_1$ Adaptive Controller for Multi-Input Multi-Output Systems in the Presence of Nonlinear Unmatched Uncertainties," *American Control Conference*, Baltimore, MD, USA, 2010, pp. 874–879.

[15] Diebel, J., "Representing attitude: Euler angles, unit quaternions, and rotation vectors." *Matrix*, Vol. 58, No. 15, 2006, pp. 1–35.

[16] Jafarnejadsani, H., and Hovakimyan, N., "Optimal Filter Design for a Discrete-Time Formulation of $\mathcal{L}_1$-Adaptive Control," *AIAA Infotech @ Aerospace*, Kissimmee, FL, USA, 2015. AIAA 2015-0119.

[17] "Flying Qualities of Piloted Aircraft," , 1997. Department of Defense Handbook. MIL-HDBK-1797.